

Long-life and high-rate $\text{Li}_3\text{V}_2(\text{PO}_4)_3/\text{C}$ nanosphere cathode materials with three-dimensional continuous electron pathways†

Cite this: *Nanoscale*, 2013, 5, 4864

Liqiang Mai,‡* Shuo Li,‡ Yifan Dong,‡ Yunlong Zhao, Yanzhu Luo and Hongmei Xu

Lithium-ion batteries (LIBs) are receiving considerable attention as storage devices in the renewable and sustainable energy developments. However, facile fabrication of long-life and high-rate cathode materials for LIBs is required to facilitate practical application. Here we report a favourable way to synthesize a $\text{Li}_3\text{V}_2(\text{PO}_4)_3/\text{C}$ nanosphere cathode with three-dimensional (3D) continuous electron pathways by synergistically utilizing polyethyleneglycol (PEG) and acetylene black for carbon coating and conductive network construction. The as-prepared cathode material has a discharge capacity of 142 mA h g^{-1} at 1 C rate, approaching its theoretical value (150 mA h g^{-1}), and can even be cycled at a rate as high as 30 C without capacity fading. After 1000 cycles at a rate of 5 C, the as-prepared material has a capacity retention of up to 83%, and can also tolerate 5000 cycles with a considerable capacity, demonstrating excellent cycling stability. Our work shows that this material has great potential for high-energy and high-power energy storage applications, and this rational method can be applied to synthesize high-performance cathode materials on a large scale.

Received 26th March 2013

Accepted 29th March 2013

DOI: 10.1039/c3nr01490h

www.rsc.org/nanoscale

Introduction

With the urgent requirements of energy storage and utilization, LIBs have attracted tremendous attention in many applications for fast charge–discharge rate, high capacity and long life-span.^{1–6} Among the candidate materials for high power LIBs, sodium super ionic conductor (NASICON) structured polyanion-based orthophosphate $\text{Li}_3\text{V}_2(\text{PO}_4)_3$ exhibits high energy and power density, thermal stability, low toxicity and low cost, and has been regarded as a prospective alternative cathode material in high power facilities such as electric vehicles, hybrid electric vehicles, and other power-supply equipment.^{7–18}

Nevertheless, $\text{Li}_3\text{V}_2(\text{PO}_4)_3$ still faces some challenges. Firstly, $\text{Li}_3\text{V}_2(\text{PO}_4)_3$ has intrinsic low electronic conductivity, which limits its applications in high rate performance. Secondly, the structure degradation during the Li^+ intercalation/

deintercalation process and the side reaction between the active material and organic electrolyte cause capacity fading and safety issues. Thirdly, the complex synthesis process and the difficulty in morphology controllability of $\text{Li}_3\text{V}_2(\text{PO}_4)_3$ limit its developments in large-scale application.^{19–21}

There have been several approaches to solve the issues listed above. Surface coating is an economic and feasible technique to improve the battery performance by virtue of modifying the surface chemistry or providing protection layers to minimize the direct contact of the active material with the electrolyte.^{22–29} Among them, carbon coating plays an important role due to the advantages arising from the unique properties of carbon, such as excellent electrical conductivity, superior chemical and electrochemical stability, unique physical properties, low cost and easy realization.^{30–32} Surface carbon coating can effectively alleviate the problem of structure degradation during cycling, giving rise to the increase of the cycling stability of $\text{Li}_3\text{V}_2(\text{PO}_4)_3$ by several orders of magnitude. Besides, the full carbon coating layer also improves the $\text{Li}_3\text{V}_2(\text{PO}_4)_3$ chemical stability as V^{3+} is an unstable valence state of vanadium.^{33–38} Simultaneously, the intrinsic low conductivity of $\text{Li}_3\text{V}_2(\text{PO}_4)_3$ could be enhanced by adding conductive agents to form a continuous conductive path in the electrode, thus promoting the rate capability.^{39–45}

Here we propose a rationally controllable synthesis of highly crystalline $\text{Li}_3\text{V}_2(\text{PO}_4)_3$ nanospheres with a uniform carbon coating layer to restrain structure degradation during cycling. Additionally, acetylene black was used as the reducing agent and the template for particle growth, as well as a three-dimensional conductive and flexible network to provide a continuous

State Key Laboratory of Advanced Technology for Materials Synthesis and Processing, WUT-Harvard Joint Nano Key Laboratory, Wuhan University of Technology, Wuhan, 430070, P. R. China. E-mail: mlq518@whut.edu.cn; Fax: +86-027-87644867; Tel: +86-027-87467595

† Electronic supplementary information (ESI) available: SEM images of samples with different PEG amounts; SEM images of acetylene black and graphite; XRD and SEM images of $\text{Li}_3\text{V}_2(\text{PO}_4)_3$ using graphite as the carbon source; TG analysis of different samples; BET analysis, the electrochemical performance and Ragone plot of samples with 20% PEG. See DOI: 10.1039/c3nr01490h

‡ Author contributions: Yifan Dong and Shuo Li performed the experiments. Liqiang Mai, Shuo Li and Yifan Dong designed the experiments, discussed the interpretation of results and co-wrote the paper. All authors discussed the results and commented on the manuscript.

electron pathway in the electrode. The uniform carbon layer and the conductive carbon network have a synergetic effect to enhance not only the cycling stability but also rate performance of $\text{Li}_3\text{V}_2(\text{PO}_4)_3$ in the application for LIBs.

Experimental

Synthesis of $\text{Li}_3\text{V}_2(\text{PO}_4)_3/\text{C}$ nanosphere cathode

For the typical synthesis of $\text{Li}_3\text{V}_2(\text{PO}_4)_3/\text{C}$ nanospheres, NH_4VO_3 , H_3PO_4 , Li_2CO_3 , polyethyleneglycol (PEG-4000) and acetylene black were used as starting materials and NH_4VO_3 , H_3PO_4 , Li_2CO_3 were in a molar ratio of 2 : 3 : 1.5. Firstly, H_3PO_4 was slowly introduced to the NH_4VO_3 solution dropwise under magnetic stirring. When a brownish-red solution was formed, Li_2CO_3 , PEG, and acetylene black were added into the solution and stirred for 20 min. The mixture was continuously stirred at 70 °C for 7 h. Then, the solution was dried at 70 °C in an air oven and pre-heated at 300 °C for 4 h in an Ar atmosphere. Finally, the pre-heated material was ground and sintered at 800 °C for 8 h under Ar flow to yield $\text{Li}_3\text{V}_2(\text{PO}_4)_3/\text{C}$ composites. Different ratios of PEG (labeled as S10, S20 and S30 for 10, 20 and 30 wt% of total mass, respectively) have been investigated. For comparison, the $\text{Li}_3\text{V}_2(\text{PO}_4)_3/\text{C}$ without PEG-4000 was prepared in the same way (labeled as S0).

Material characterization

X-ray diffraction (XRD) measurement was performed to investigate the crystallographic information using a Bruker D8 Advance X-ray diffractometer with a non-monochromated Cu $K\alpha$ X-ray source. Scanning electron microscopy (SEM) images were collected with a JEOL JSM-7100F at an acceleration voltage of 15 kV. Transmission electron microscopic (TEM) and high resolution transmission electron microscopic (HRTEM) images were recorded with a JEOL JEM-2100F STEM/EDS microscope. Brunauer–Emmett–Teller (BET) surface areas were measured using an ASAP 3020M instrument to measure the adsorption of nitrogen at −209 °C. Thermogravimetry analysis (TG) was performed using a Netzsch STA 449F3 simultaneous thermal analyzer at a heating rate of 10 °C min^{−1} in air.

Electrochemical measurements

The electrochemical properties were tested with 2025 coin cells assembled in a glove box filled with pure argon gas. Lithium pellets were used as the anode, a 1 M solution of LiPF_6 in ethylene carbon (EC)–dimethyl carbonate (DEC) (1 : 1 w/w) was used as the electrolyte, and the cathode electrodes were produced with 70% $\text{Li}_3\text{V}_2(\text{PO}_4)_3$ nanoparticle active material, 20% acetylene black and 10% poly(tetrafluoroethylene) and compressed into pellets and placed on a Cu current collector. Galvanostatic charge–discharge measurement was performed in the potential range of 3.0 to 4.5 V vs. Li/Li^+ with a multi-channel battery testing system (LAND CT2001A). Cyclic voltammetry (CV) and electrochemical impedance spectra (EIS) were measured with an electrochemical workstation (Autolab PGSTAT 302 and CHI 760D).

Results and discussion

The schematic to realize the synergetic function of the carbon network and carbon coating layer is illustrated in Fig. 1. The carbon network, which is formed from acetylene black, provides a facile and continuous pathway for electron transport, leading to enhanced conductivity of the electrode; the carbon layer, which is developed from PEG calcinations, can prohibit the structure degradation during lithium diffusion into the active material, resulting in better electrochemical stability. This synergetic effect may promote the performance of the $\text{Li}_3\text{V}_2(\text{PO}_4)_3$ cathode material and make it a promising candidate in high-rate and long-life energy storage applications.

To determine the phase structure of the products, XRD measurements were conducted (Fig. 2). All the diffraction peaks of the patterns of $\text{Li}_3\text{V}_2(\text{PO}_4)_3$ nanoparticles with different PEG amounts can be readily indexed to a well-defined monoclinic structure of pure $\text{Li}_3\text{V}_2(\text{PO}_4)_3$, corresponding well to the previously reported literature.⁴⁶ The consistent peak position shows that the addition of PEG has no influence on the phase structure of $\text{Li}_3\text{V}_2(\text{PO}_4)_3/\text{C}$, and acetylene black plays the role in reducing V^{5+} to V^{3+} . No evidence of the impurity peaks or characteristic peaks of crystallized carbon is observed, indicating that the products are of high purity and both the carbon layer and conductive carbon network are amorphous.

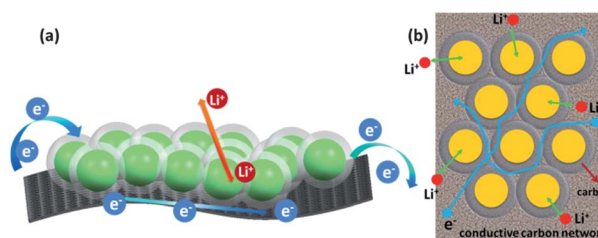


Fig. 1 Schematic illustration of $\text{Li}_3\text{V}_2(\text{PO}_4)_3$ nanospheres with a carbon coating layer and continuous carbon network (a) and top cross-section view (b).

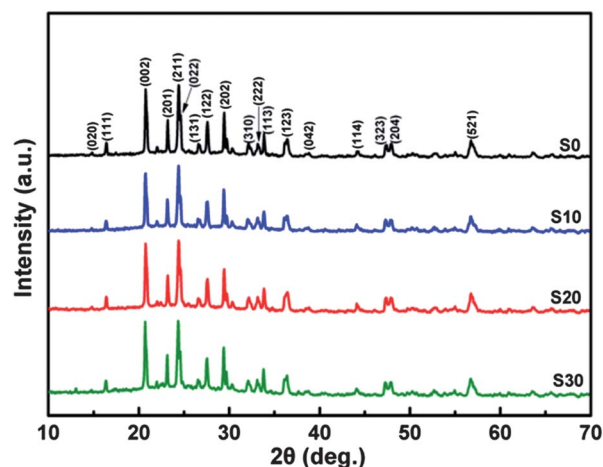


Fig. 2 XRD patterns of S0, S10, S20 and S30 for 0, 10, 20 and 30 wt% PEG of total mass, respectively.

The prepared S0, S10, S20 and S30 materials show a sphere-like morphology with pores between the nanospheres in SEM images (ESI Fig. S1†). It is remarkable that the sphere-like structures for all the coated and pristine materials are kept through the calcinations at 800 °C, and the dominant factor in forming the sphere-like $\text{Li}_3\text{V}_2(\text{PO}_4)_3$ particles is investigated. During the calcination process, PEG forms a homogeneous carbon layer (the thickness can be tuned by adjusting the PEG amount), and the carbon layer can restrain the particle growth and maintain the $\text{Li}_3\text{V}_2(\text{PO}_4)_3$ particles at the nanoscale. Acetylene black is chosen as the carbon source due to its physical morphology of finely divided pellets or powder with high surface-to-volume ratio (ESI Fig. S2a†), and it acts as a template in our synthesis process to control the morphology of $\text{Li}_3\text{V}_2(\text{PO}_4)_3$ to sphere morphology. In the control experiment, acetylene black was replaced by graphite with the same amount. The phase of the product is still pure $\text{Li}_3\text{V}_2(\text{PO}_4)_3$ (ESI Fig. S3a†), while the SEM images show that graphite-induced $\text{Li}_3\text{V}_2(\text{PO}_4)_3$ products are nanosheets (ESI Fig. S3b†), similar to the laminar structure of graphite (ESI Fig. S2b†). This indicates that the carbon source plays a dominant role in controlling the morphology of the $\text{Li}_3\text{V}_2(\text{PO}_4)_3$ particles. Besides, the excess acetylene black can form a continuous carbon network between the $\text{Li}_3\text{V}_2(\text{PO}_4)_3$ particles, which enhances the electron conductivity of the material and may greatly improve the rate performance. The diameters of the nanospheres for S10, S20 and S30 are 40–60 nm with good uniformity, while for S0 without PEG, there exists some distinct agglomeration and large grains, indicating the necessity of PEG in controlling and optimizing the morphology and surface uniformity of $\text{Li}_3\text{V}_2(\text{PO}_4)_3$ particles.

To further investigate the function of PEG in forming the coating layer, HRTEM and TEM images of S0, S10, S20 and S30 are shown in Fig. 3. For S0 without PEG, the nanoparticles have

irregular morphologies with little amorphous carbon on the surface, while for S10, S20 and S30, the samples all have sphere-like morphologies with fine amorphous carbon coating layers. The thicknesses of coating layers are uniform and are around 3, 5 and 7 nm, corresponding to the different PEG amounts for S10, S20 and S30, respectively. TG analysis also indicates the carbon amount for each sample varies by adjusting the layer thickness (ESI Fig. S4†). From the TEM images (Fig. 3 insets), some pores can be observed between the nanospheres as the spheres are piled together. These pores functionalize a relatively large surface-to-volume ratio of the nanospheres with a BET surface area of $20.41 \text{ m}^2 \text{ g}^{-1}$ (ESI Fig. S5†), and the porous structure of the material significantly increases the active sites to contact the electrolyte, thus promoting the lithium intercalation/deintercalation process.

To evaluate the influence of the coating layer on the electrochemical performance of $\text{Li}_3\text{V}_2(\text{PO}_4)_3$, electrochemical tests were carried out for S0, S10, S20 and S30. CV results for samples S0, S10, S20 and S30 are shown in Fig. 4a. The voltammograms were measured at a sweep rate of 0.1 mV s^{-1} in the potential range of 3.0 to 4.5 V vs. Li/Li^+ at room temperature. It is obvious that S20 has a larger curve area and higher redox peak current than other samples, suggesting that S20 has the highest capacity and the fastest kinetics for Li ion insertion/extraction due to the moderate amount of carbon coating.

S20 is used as an example to explain the electrochemical process. All of these peaks originate from the phase transitions between $\text{Li}_{3-x}\text{V}_2(\text{PO}_4)_3$ components with different x values ($0 < x < 2$). There are three oxidation peaks and three reduction peaks. The first two oxidation peaks around 3.63 and 3.72 V correspond to the removal of the first Li in two steps, since there is an ordered $\text{Li}_{2.5}\text{V}_2(\text{PO}_4)_3$ phase. However, the second Li is extracted through one step around 4.14 V, corresponding to the complete oxidation of V^{3+} to V^{4+} . The three reduction peaks located around 3.99, 3.62, 3.54 V are attributed to the reinsertion of the two Li^+ ions, associated with the $\text{V}^{4+}/\text{V}^{3+}$ redox couple.^{47,48}

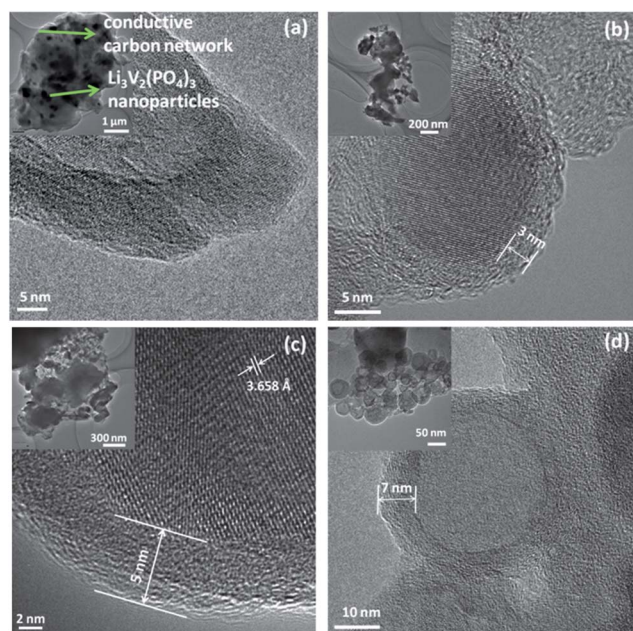


Fig. 3 Typical HRTEM images of (a) S0, (b) S10, (c) S20 and (d) S30. (Insets a–d: TEM images of S0, S10, S20 and S30.)

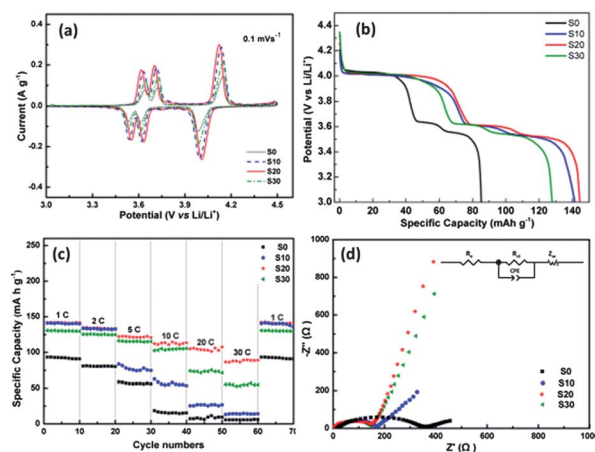


Fig. 4 Electrochemical properties of S0, S10, S20 and S30. (a) CV curves at a sweep rate of 0.1 mV s^{-1} in the potential range of 3.0 to 4.5 V vs. Li/Li^+ . (b) The discharge curves at 1 C of the samples. (c) Discharge capacities of the samples at various current rates from 1 to 30 C. (d) AC-impedance spectra of the samples respectively.

Fig. 4b presents the discharge profiles of the samples at a rate of 1 C (1 C corresponds to 150 mA g^{-1}) over a potential window of 3–4.5 V. It can be clearly seen that all the samples have three discharge plateaus around 3.99, 3.62 and 3.54 V corresponding well with the reduction peaks in the CV curve, which are identified as the two-phase transition processes of $\text{LiV}_2(\text{PO}_4)_3 \rightarrow \text{Li}_2\text{V}_2(\text{PO}_4)_3 \rightarrow \text{Li}_{2.5}\text{V}_2(\text{PO}_4)_3 \rightarrow \text{Li}_3\text{V}_2(\text{PO}_4)_3$ during the electrochemical reactions. The initial discharge capacity of S20 is 145 mA h g^{-1} , higher than 85, 141 and 128 mA h g^{-1} for S0, S10 and S30, respectively.

To further understand the high rate performance of the samples, the batteries were charged and discharged at different rates ranging from 1 C to 30 C in the potential range of 3.0–4.5 V (Fig. 4c). The S20 cathode delivered the highest discharge capacities of 142, 135, 122, 112, and 105 mA h g^{-1} at current rates of 1, 2, 5, 10 and 20 C, respectively. Remarkably, even after 50 cycles, the capacity at a current rate of 30 C still reaches 87 mA h g^{-1} . In addition, after this high-rate measurement, the battery with the S20 is able to recover to a high capacity of 142 mA h g^{-1} at 1 C without decreasing.

It can be obviously observed that the rate capability of the PEG-assisted $\text{Li}_3\text{V}_2(\text{PO}_4)_3$ composites is much better than S0 without PEG. At low current rates (1 C and 2 C), specific capacities of S20 and S10 are almost the same while the capacity of S30 is lower, due to its relatively low active material ratio of $\text{Li}_3\text{V}_2(\text{PO}_4)_3$ in S30 with high carbon content; at higher current rates (5 C and above), the specific capacity of S10 is lower than those of S20 and S30 because the thin carbon layer cannot effectively restrain the structure degradation and the surface conductivity is still not high enough.⁴⁹ This rate performance investigation indicates the excellent structural stability and rate capability of carbon coated $\text{Li}_3\text{V}_2(\text{PO}_4)_3$ nanoparticles, and S20 exhibits better electrochemical performance than S10 and S30 as a result of the moderate carbon layer thickness due to the proper PEG amount.

The EIS of $\text{Li}_3\text{V}_2(\text{PO}_4)_3$ electrode materials were measured at the same discharge state about 4.1 V after 50 cycles at 0.5 C (Fig. 4d). All the profiles exhibit a semicircle in the high-frequency region and a straight line in the low-frequency region. The semicircle is ascribed to the lithium ion migration through the interface between the surface layer of the particles and the electrolyte. By comparing the R_{ct} (charge-transfer resistance), it is found that the charge transfer resistance of S0 is much higher than the other samples, indicating that the electrical conductivity of the material is very low due to the absence of the carbon layer and particle size inhomogeneity. The straight line is attributed to the diffusion of lithium ions in the bulk of the electrode material, and the diffusion coefficient values of the lithium ions (D) can be calculated using the equation $D = 0.5(RT/AF^2\sigma_w C)^2$, where R is the gas constant, T is the temperature, A is the area of the electrode surface, F is Faraday's constant, and C is the molar concentration of Li^+ ions. The calculated lithium diffusion coefficient values for S0, S10, S20 and S30 are 3.56×10^{-13} , 2.31×10^{-11} , 1.8×10^{-10} and $1.18 \times 10^{-10} \text{ cm}^2 \text{ s}^{-1}$, respectively. It can be seen that the lithium diffusion coefficient of S0 is much lower, while S20 possesses the highest lithium diffusion coefficient among the samples with carbon layer, and is about three orders of magnitude higher than

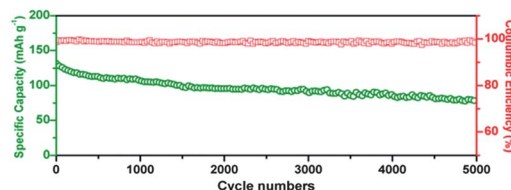


Fig. 5 Charge-discharge cycling performance of the S20 cathode at 5 C rate for 5000 cycles.

S0. The difference in the value may be attributed to the fact that a low amount of PEG might form a thin but hardly a full coating layer on the surface of the electrode; while an excessively thick carbon coating layer would act as a barrier for Li^+ diffusion.²⁵

As S20 exhibits the best performance among all the samples, it was cycled for 5000 cycles at a current density of 5 C to investigate the long-life performance (Fig. 5). The initial discharge capacity of S20 is 132 mA h g^{-1} , after 1000 cycles, the specific capacity is still maintained at 109 mA h g^{-1} , 83% of the initial capacity. Even after 5000 cycles, the S20 still retains the capacity of 79 mA h g^{-1} . The coulombic efficiency can reach up to 99% in the overall battery operation, indicating good reversibility of S20. This optimum performance demonstrates the successful fabrication of S20 by using a moderate amount of morphology-optimized agent PEG and the continuous network of acetylene black. Due to the synergetic effect of both increasing the cycling stability and rate capability, the impressive electrochemical performance of $\text{Li}_3\text{V}_2(\text{PO}_4)_3$ can be achieved. The cycle life of 5000 cycles is longer than those of the reported long-life electrode materials for power batteries such as LiMn_2O_4 of 2000 cycles³⁴ and LiFePO_4 of around 1000 cycles.^{40,50}

The specific energy and specific power of S20 are shown in the Ragone plot (ESI Fig. S7†). The S20 exhibited a specific energy of 537 W h kg^{-1} at 1 C rate, and remarkably, it can deliver a specific power of 14.5 kW kg^{-1} while retaining a specific energy of 350 W h kg^{-1} . Our as-synthesized nanomaterials have a comparable specific power and energy density, and may be used for promising electrochemical energy-storage devices such as LIBs with both high-power and high-energy densities.

The excellent cycling stability is because the PEG-induced carbon coating layer can restrain the structure degradation during cycling, and can prohibit the side reaction with the electrolyte, thus greatly enhancing the cycling stability. Moreover, PEG has the function to optimize the morphology uniformity of the particles. It was found that 20% PEG is the best amount for carbon coating (5 nm layer thickness), which may result from the fact that the 5 nm thick carbon layer can effectively restrain the structure degradation without significantly decreasing the specific capacity as carbon is a low-capacity component in the cathode. In contrast, 3 nm carbon layers in S10 cannot effectively restrain the structure degradation or improve surface conductivity, leading to poorer cycling stability; and 7 nm carbon layers may result in less ratio of active materials, thus leading to a relatively lower specific capacity.

The carbon source has a significant influence on the morphology, structure and electrochemical performance of the resulting nanomaterial. As acetylene black has a morphology of

finely divided pellets, it acts as a template for crystal growth of $\text{Li}_3\text{V}_2(\text{PO}_4)_3$, resulting in the sphere-like nanoparticles. Besides, the pores between the piled spheres permit the large surface-to-volume ratio to contact the electrolyte and leads to more active sites for lithium intercalation/deintercalation. Additionally, the excess carbon source in the electrode can act as a conductive carbon network, thus significantly enhancing the rate performance.

In our design, the unique porous structure of carbon-coated $\text{Li}_3\text{V}_2(\text{PO}_4)_3$ with a continuous carbon network brings some synergetic benefits in increasing the cycling stability and rate performance. First, the morphology of $\text{Li}_3\text{V}_2(\text{PO}_4)_3$ can be controlled with different carbon sources, and the excess carbon source forms a continuous network for electron pathways. Second, the carbon layer is beneficial in suppressing the structure degradation and side reaction during cycling, which greatly enhances the cycling stability.

Conclusions

In summary, sphere-like $\text{Li}_3\text{V}_2(\text{PO}_4)_3$ nanoparticles using acetylene black as the template and PEG as the surface modification reactant have been prepared. The prepared $\text{Li}_3\text{V}_2(\text{PO}_4)_3$ nanospheres exhibit impressive rate capability and cycling stability resulting from the continuous carbon network and carbon coating layer. When cycled at a rate as high as 30 C the capacity can reach up to 87 mA h g^{-1} , and after 5000 cycles at a rate of 5 C the capacity is still maintained at 79 mA h g^{-1} . The moderate carbon layer on $\text{Li}_3\text{V}_2(\text{PO}_4)_3$ nanoparticles suppresses the particle degradation and the side reaction during cycling, resulting in excellent cycling performance. The optimum design of the continuous network for electron pathways enables high-rate performance. Moreover, the morphology can be controlled using different carbon sources, and the thickness of the carbon layer can be tuned by adjusting the PEG amount. In addition, this feasible synthesized route provides a rational method to enhance the electrochemical performance of electrode materials, and may lead to the great development of large-scale synthesis of safe and stable, high-energy and high-power materials for energy storage.

Acknowledgements

This work was supported by the National Basic Research Program of China (2013CB934103, 2012CB933003), the National Natural Science Foundation of China (51272197, 51072153), the Program for New Century Excellent Talents in University (NCET-10-0661), the Fundamental Research Funds for the Central Universities (2012-II-001) and the International Science and Technology Cooperation (2013DFA50840).

Notes and references

- 1 S. Chu and A. Majumdar, *Nature*, 2012, **488**, 294–303.
- 2 J. Tarascon and M. Armand, *Nature*, 2001, **414**, 359–367.
- 3 N. S. Choi, Z. Chen, S. A. Freunberger, X. Ji, Y. K. Sun, K. Amine, G. Yushin, L. F. Nazar, J. Cho and P. G. Bruce, *Angew. Chem., Int. Ed.*, 2012, **51**, 9994–10024.
- 4 M. Armand and J. M. Tarascon, *Nature*, 2008, **451**, 652–657.
- 5 L. Q. Mai, Q. L. Wei, Q. Y. An, X. C. Tian, Y. L. Zhao, X. Xu, L. Xu, L. Chang and Q. J. Zhang, *Adv. Mater.*, 2013, DOI: 10.1002/adma.201205185.
- 6 B. Scrosati, J. Hassoun and Y. K. Sun, *Energy Environ. Sci.*, 2011, **4**, 3287–3295.
- 7 P. Barpanda, S. Nishimura and A. Yamada, *Adv. Energy Mater.*, 2012, **2**, 841–859.
- 8 J. Gopalakrishnan and K. K. Rangan, *Chem. Mater.*, 1992, **4**, 745–747.
- 9 A. Shukla and T. Prem Kumar, *Curr. Sci.*, 2008, **94**, 314–331.
- 10 N. A. Chernova, M. Roppolo, A. C. Dillon and M. S. Whittingham, *J. Mater. Chem.*, 2009, **19**, 2526–2552.
- 11 M. S. Whittingham, *Chem. Rev.*, 2004, **104**, 4271–4302.
- 12 Y. U. Park, D. H. Seo, B. Kim, K. P. Hong, H. Kim, S. Lee, R. A. Shakoor, K. Miyasaka, J. M. Tarascon and K. Kang, *Sci. Rep.*, 2012, **2**, n704.
- 13 B. L. Cushing and J. B. Goodenough, *J. Solid State Chem.*, 2001, **162**, 176–181.
- 14 J. B. Goodenough and K. S. Park, *J. Am. Chem. Soc.*, 2013, **135**, 1167–1176.
- 15 Z. Gong and Y. Yang, *Energy Environ. Sci.*, 2011, **4**, 3223–3242.
- 16 V. Palomares, P. Serras, I. Villaluenga, K. B. Hueso, J. Carretero-González and T. Rojo, *Energy Environ. Sci.*, 2012, **5**, 5884–5901.
- 17 S. P. Ong, V. L. Chevrier, G. Hautier, A. Jain, C. Moore, S. Kim, X. Ma and G. Ceder, *Energy Environ. Sci.*, 2011, **4**, 3680–3688.
- 18 Y. Zhu, Y. Xu, Y. Liu, C. Luo and C. Wang, *Nanoscale*, 2013, **5**, 780–787.
- 19 G. Yang, H. Liu, H. Ji, Z. Chen and X. Jiang, *J. Power Sources*, 2010, **195**, 5374–5378.
- 20 X. Du, W. He, X. Zhang, Y. Yue, H. Liu, D. Min, X. Ge and Y. Du, *J. Mater. Chem.*, 2012, **22**, 5960–5969.
- 21 H. Wang, Y. Liar, C. Huang, Y. Zhong and S. Liu, *J. Power Sources*, 2012, **208**, 282–287.
- 22 Z. Chen, Y. Qin, K. Amine and Y. K. Sun, *J. Mater. Chem.*, 2010, **20**, 7606–7612.
- 23 S. Li, C. H. Han, L. Q. Mai, J. H. Han, X. Xu and Y. Q. Zhu, *Int. J. Electrochem. Sci.*, 2011, **6**, 4504–4513.
- 24 L. Q. Mai, F. Dong, X. Xu, Y. Z. Luo, Q. Y. An, Y. L. Zhao, J. Pan and J. N. Yang, *Nano Lett.*, 2013, **13**, 740–745.
- 25 L. Shen, H. Li, E. Uchaker, X. Zhang and G. Cao, *Nano Lett.*, 2012, **12**, 5673–5678.
- 26 D. W. Kim, I. S. Hwang, S. J. Kwon, H. Y. Kang, K. S. Park, Y. J. Choi, K. J. Choi and J. G. Park, *Nano Lett.*, 2007, **7**, 3041–3045.
- 27 L. Q. Mai, X. Xu, C. H. Han, Y. Z. Luo, L. Xu, Y. M. Wu and Y. L. Zhao, *Nano Lett.*, 2011, **11**, 4992–4996.
- 28 L. Su, Y. Jing and Z. Zhou, *Nanoscale*, 2011, **3**, 3967–3983.
- 29 D. Guan, J. A. Jeevarajan and Y. Wang, *Nanoscale*, 2011, **3**, 1465–1469.
- 30 H. Li and H. Zhou, *Chem. Commun.*, 2011, **48**, 1201–1217.
- 31 H. Ni, J. Liu and L. Z. Fan, *Nanoscale*, 2013, **5**, 2164–2168.
- 32 L. Wang, J. Liang, Y. Zhu, T. Mei, X. Zhang, Q. Yang and Y. Qian, *Nanoscale*, 2013, DOI: 10.1039/c3nr00353a.

- 33 M. Ren, Z. Zhou, X. Gao, W. Peng and J. Wei, *J. Phys. Chem. C*, 2008, **112**, 5689–5693.
- 34 S. Lee, Y. Cho, H. K. Song, K. T. Lee and J. Cho, *Angew. Chem., Int. Ed.*, 2012, **51**, 8748–8752.
- 35 C. Sun, S. Rajasekhara, Y. Dong and J. B. Goodenough, *ACS Appl. Mater. Interfaces*, 2011, **3**, 3772–3776.
- 36 J. Qian, M. Zhou, Y. Cao, X. Ai and H. Yang, *J. Phys. Chem. C*, 2010, **114**, 3477–3482.
- 37 H. Liu, G. Yang, X. Zhang, P. Gao, L. Wang, J. Fang, J. Pinto and X. Jiang, *J. Mater. Chem.*, 2012, **22**, 11039–11047.
- 38 J. Su, X. L. Wu, J. S. Lee, J. Kim and Y. G. Guo, *J. Mater. Chem. A*, 2013, **1**, 2508–2514.
- 39 S. Luo, K. Wang, J. Wang, K. Jiang, Q. Li and S. Fan, *Adv. Mater.*, 2012, **24**, 2294–2298.
- 40 J. F. von Bülow, H. L. Zhang and D. E. Morse, *Adv. Energy Mater.*, 2012, **2**, 309–315.
- 41 M. Chen, C. Du, B. Song, K. Xiong, G. Yin and P. Zuo, *J. Power Sources*, 2012, **223**, 100–106.
- 42 A. Pan, J. Liu, J. G. Zhang, W. Xu, G. Cao, Z. Nie, B. W. Arey and S. Liang, *Electrochem. Commun.*, 2010, **12**, 1674–1677.
- 43 X. L. Wu, L. Y. Jiang, F. F. Cao, Y. G. Guo and L. J. Wan, *Adv. Mater.*, 2009, **21**, 2710–2714.
- 44 H. Huang, S. C. Yin, T. Kerr, N. Taylor and L. F. Nazar, *Adv. Mater.*, 2002, **14**, 1525–1528.
- 45 H. Liu, P. Gao, J. Fang and G. Yang, *Chem. Commun.*, 2011, **47**, 9110–9112.
- 46 S. C. Yin, H. Grondy, P. Strobel, M. Anne and L. Nazar, *J. Am. Chem. Soc.*, 2003, **125**, 10402–10411.
- 47 X. Zhu, Y. Liu, L. Geng and L. Chen, *J. Power Sources*, 2008, **184**, 578–582.
- 48 L. Wang, X. Zhou and Y. Guo, *J. Power Sources*, 2010, **195**, 2844–2850.
- 49 J. Wang and X. Sun, *Energy Environ. Sci.*, 2012, **5**, 5163–5185.
- 50 C. Wu, G. Cao, H. Yu, J. Xie and X. Zhao, *J. Phys. Chem. C*, 2011, **115**, 23090–23095.